



HAL
open science

Effects of helium irradiation on fine grained β -SiC synthesized by spark plasma sintering

S. Gavarini, J. Baillet, N. Millard-Pinard, V. Garnier, C. Peaucelle, X. Jaurand, C. Bernard, R. Rapegno, S. Cardinal, C. Dalverny, et al.

► To cite this version:

S. Gavarini, J. Baillet, N. Millard-Pinard, V. Garnier, C. Peaucelle, et al.. Effects of helium irradiation on fine grained β -SiC synthesized by spark plasma sintering. *Journal of the European Ceramic Society*, 2020, 40, pp.1-11. 10.1016/j.jeurceramsoc.2019.09.018 . cea-02293252

HAL Id: cea-02293252

<https://cea.hal.science/cea-02293252>

Submitted on 21 Dec 2021

HAL is a multi-disciplinary open access archive for the deposit and dissemination of scientific research documents, whether they are published or not. The documents may come from teaching and research institutions in France or abroad, or from public or private research centers.

L'archive ouverte pluridisciplinaire **HAL**, est destinée au dépôt et à la diffusion de documents scientifiques de niveau recherche, publiés ou non, émanant des établissements d'enseignement et de recherche français ou étrangers, des laboratoires publics ou privés.



Distributed under a Creative Commons Attribution - NonCommercial 4.0 International License

1 Introduction

2 Nuclear industry is looking to develop new materials able to withstand increasingly hostile environments.
3 Because of its remarkable properties (creep and oxidation resistance [1-3], radiation tolerance [4-8]), silicon
4 carbide is under investigation as cladding with enhanced tolerance for light water reactors [9-16], as well as
5 cladding for GenIV nuclear plants [9-11, 17-18]. For nuclear fusion [9-10], the addition of SiC in the form of a
6 thin layer on the metallic structures (W [19] or Eurofer [20], i.e. Reduced Activation Ferritic Martensitic steel),
7 should enable better control of the tritium inventory (diffusion barrier limiting tritium losses). It should also
8 improve corrosion resistance in the case of SiC inserts in tritium blankets where the liquid metal, PbLi, circulates
9 [20]. For all the above-mentioned nuclear applications, the (n,α) nuclear transmutation reaction inevitably
10 introduces numerous atomic helium atoms in the SiC. The He/dpa production rate in SiC is reported to be 2.5
11 appm/dpa for typical fission neutron spectra [21-22]. In a fusion reactor, SiC will be exposed not only to a high
12 irradiation dose (up to 200 dpa), but also high helium generation rates, i.e. 70 appm/dpa in the reactor, 130
13 appm/dpa for the first wall [3, 23-25], and about 16,000 appm/yr at 10 MW/m² [26]. A rapid calculation leads to
14 typical helium concentrations of the order of 0.05 at.% for fuel components in fission reactors and about 2.5 at.%
15 (and even greater) for structural materials in fusion reactors.

16 Linez et al. [27] have shown experimentally that helium preferentially occupies tetrahedral interstitial
17 sites after implantation at room temperature in 6H-SiC. After annealing at 400 °C, a migration of helium to the
18 silicon vacancies and silicon and carbon bi-vacancies is observed. Due to the low solubility of He atoms in SiC, a
19 certain concentration of He atoms that are trapped in the matrix in the form of helium-vacancy clusters would form
20 bubbles upon annealing [28-29]. These bubbles can cause degradation of the material properties [16, 30-31], such
21 as the phenomenon of He embrittlement, microstructure evolution, blistering, volume swelling and deleterious
22 effects on thermal properties.

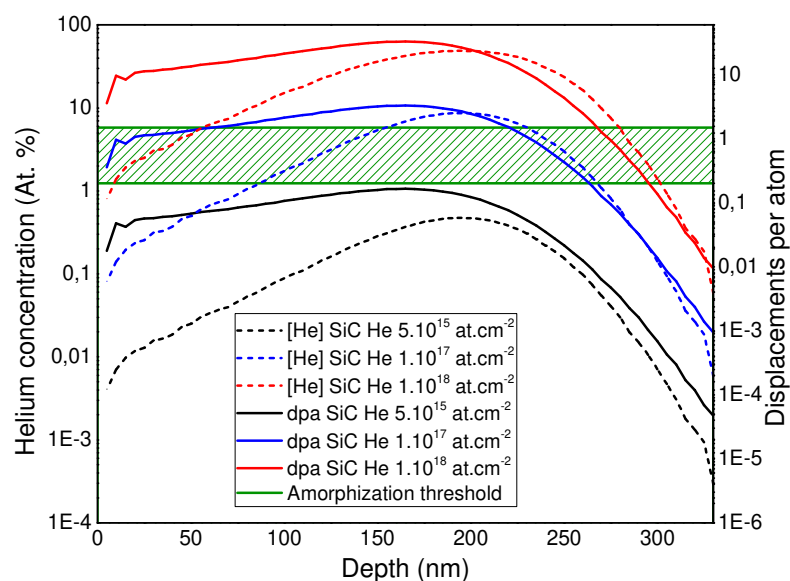
23 In the absence of suitable fission or fusion neutron test facilities capable of achieving the high neutron
24 fluences expected in advanced reactors, ion implantation and irradiation techniques can be used to investigate the
25 effect of high helium content and high irradiation doses in SiC. Ion implantation with helium ions has two
26 advantages. First, it results in a well-known helium concentration profile. Secondly, the production and
27 accumulation of defects due to the implantation can lead to amorphization and chemical disordering, as well as
28 drive the nucleation and growth of helium bubbles. Using these techniques, the threshold for helium bubble
29 formation at room temperature has been determined by several authors [30, 32-35]. These concentrations vary
30 between 1.7 and 8.0 at. %. As an illustration, Zinkle et al. [30] observed bubble formation in 3C-SiC (β -SiC) at a
31 concentration of about 4 at. % after irradiation with a 1 MeV He⁺ ion beam at room temperature. This author also
32 conducted studies at higher fluence and was also able to observe the formation of blisters and the beginning of
33 exfoliation at a concentration of about 20 at. %. Using transmission electron microscopy (TEM), only nanobubbles
34 were revealed in this study which did not include complete chemical analyses (oxidation, composition evolution,
35 helium profiles). Note that SiC blistering under light ion implantation has been also extensively described for the
36 needs of smart cut treatments that typically combine irradiation and then annealing [36]. The dependence of SiC
37 radiation resistance on irradiation species was underlined by several authors [37-38]. For example, Jamison et al.
38 [38] showed that irradiation with 1 MeV Kr ions resulted in a lower dose to amorphization if compared with lighter
39 species.

1 β -SiC specimens were synthesized by spark plasma sintering (SPS) to obtain fine microstructures with
 2 grain size below 100 nm. The synthesis and irradiation protocols are described in the first section. The second
 3 section describes the modifications induced by helium irradiation. The phenomena observed are discussed in a
 4 third section, which includes a comparison with previous results obtained on SiC [39] implanted with xenon, and
 5 TiC [40] implanted with helium at comparable fluencies.

6 2. Experimental

7 SiC samples were obtained by Spark Plasma Sintering, starting from nanopowder synthesized by laser
 8 pyrolysis. The complete protocol has been described extensively elsewhere and hence is not detailed here [39, 41].
 9 Sintered bodies exhibit grains of size comprised between 20 and 130 nm, with an average grain size near 60 nm.
 10 The relative density is found to be near 94 %, meaning that the material has some porosity that is visible on the
 11 surface after polishing. A chemical analysis was done by Ion beam analysis and the final stoichiometry was found
 12 to be $\text{SiC}_{1.02}\text{O}_{0.1}$. Thin cross sections were prepared by Focused Ion Beam (FIB) to allow TEM observations.

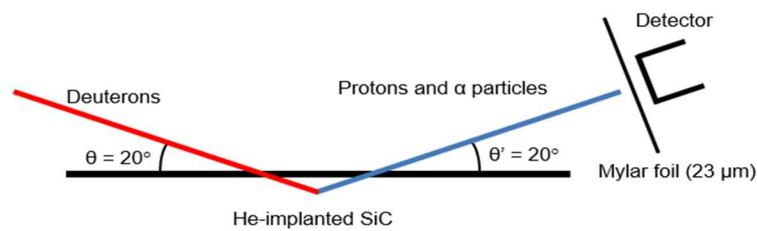
13 Three helium fluencies were used for implantation: $5 \times 10^{15} \text{ at.cm}^{-2}$ (He beam current density $i = 0.25$
 14 $\mu\text{A.cm}^{-2}$), $1 \times 10^{17} \text{ at.cm}^{-2}$ ($i = 2.5 \mu\text{A.cm}^{-2}$) and $1 \times 10^{18} \text{ at.cm}^{-2}$ ($i = 5 \mu\text{A.cm}^{-2}$). Hereafter, these fluencies are termed
 15 as Φ_1, Φ_2, Φ_3 respectively. The sample holder is kept cold during implantation by a circulation of water and helium
 16 ions are accelerated to an energy of 30 keV under a vacuum of nearly 10^{-6} mbar . Damage and nominal He
 17 concentrations were calculated using the Stopping Range of Ions in Matter (SRIM-2013) Monte Carlo computer
 18 code [42]. DPA was calculated using the ‘Quick’ Kinchin-Pease option of SRIM for 1 000 000 ions with a
 19 displacement energy of 35 eV for Si and 21 eV for C [43] with lattice and surface binding energies set to 0 eV.
 20 The results are shown in Fig. 1. The dpa range commonly accepted in the literature as that corresponding to the
 21 SiC amorphization threshold is also indicated in Fig. 1 [30]. Note that this threshold can vary according to
 22 irradiation ion species, irradiation temperature and microstructure [44].



23

1 *Figure 1: Helium depth profiles and corresponding dpa profiles, deduced from SRIM-2008[®] simulations, for the three fluences Φ_1*
2 *(low fluence), Φ_2 (intermediate fluence) and Φ_3 (high fluence).*

3 After implantation, the helium content was determined using the $^3\text{He} (d, p) ^4\text{He}$ nuclear reaction
4 characterized by a wide resonance centered on $E_d = 450 \text{ keV}$ [45]. The incident deuteron beam impinges on the
5 sample surface at an angle of 20° (Fig. 2), and a mylar foil with a thickness of $23 \mu\text{m}$ is placed in front of a Si
6 detector to block the forward scattered or recoiled particles, except protons and α particles from the $^3\text{He} (d, p) \alpha$
7 reaction. The incident deuteron energy was set at 0.6 MeV in order to reach 0.45 MeV around the maximum
8 theoretical helium concentration.



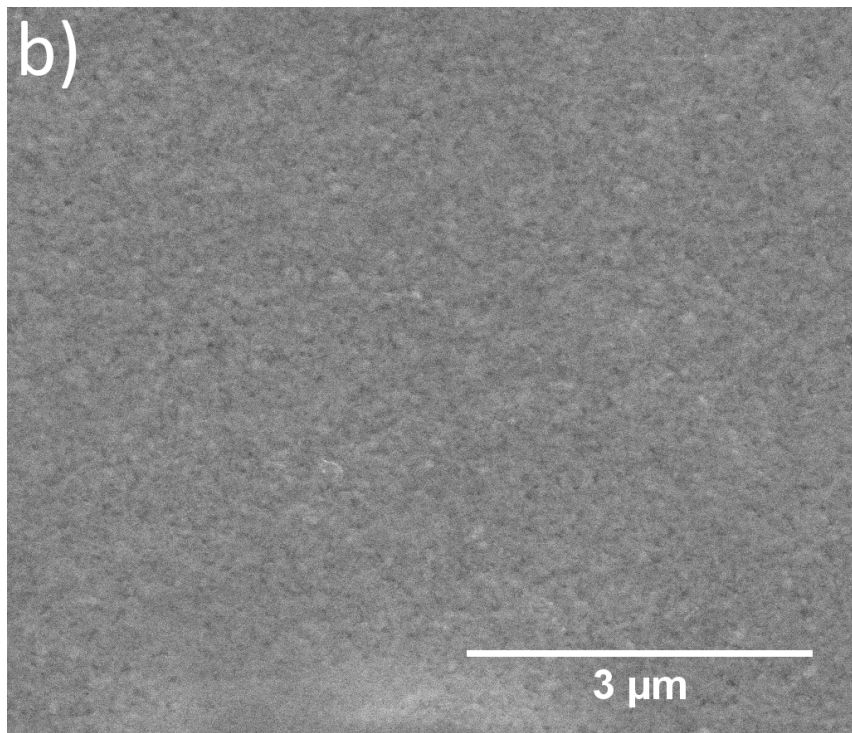
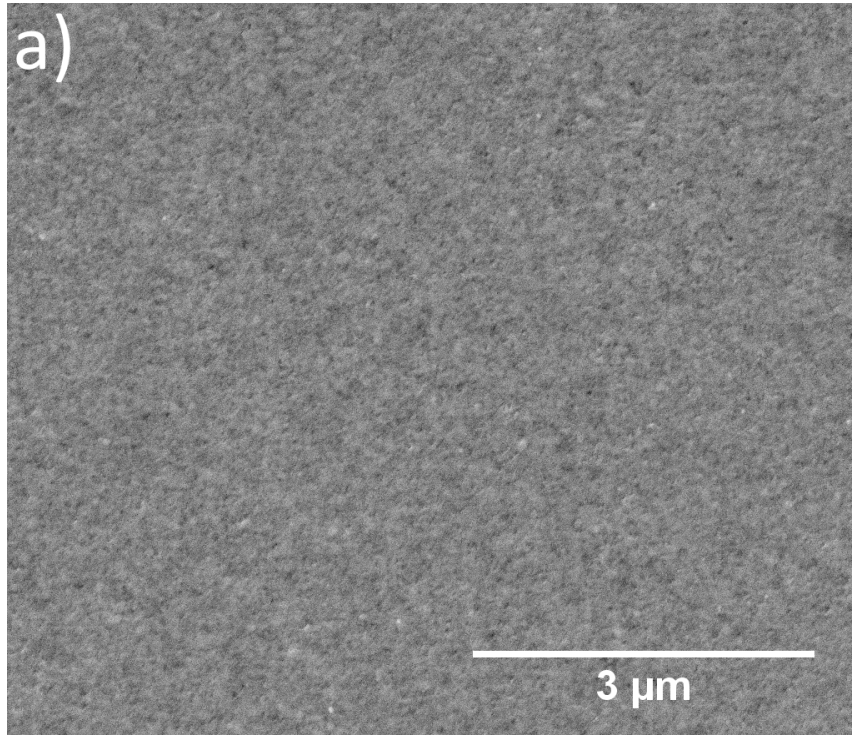
9
10 *Figure 2: Geometry used for NRA analysis.*

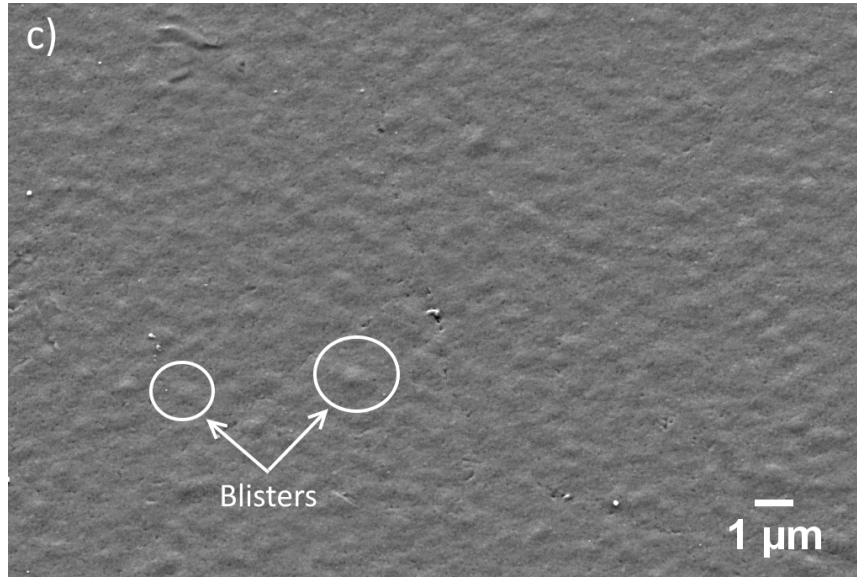
11 The evolution of the sample surface morphology was followed by SEM (FEI[®] Quanta 250 FEG ESEM).
12 Cross-sections prepared by FIB were observed by TEM (Jeol[®]2100F). Three modes were used for these
13 observations: Bright field, Selected Area electron diffraction (SAED) and Scanning TEM (STEM) with a High
14 Angle Annular Dark Field detector (HAADF), coupled with EDX analysis (elemental mapping).

15 3. Results

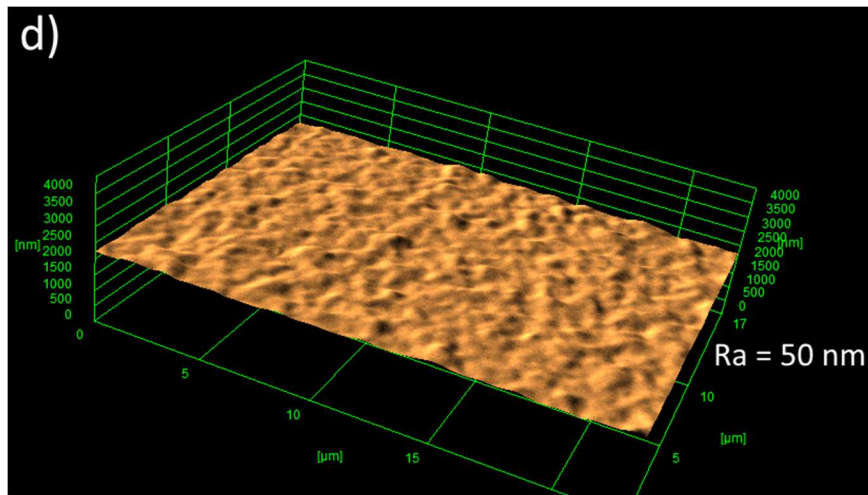
16 3.1 Surface morphology and structure

17 The surface of the SiC pellets was observed by SEM after ion implantation (Fig. 3). No visible
18 modification occurred after irradiation at Φ_1 and Φ_2 , and the images of the surface shown in Fig. 3a and 3b are
19 very similar to those obtained before irradiation. For Φ_3 , blisters of $< 1 \mu\text{m}$ formed on the surface (Fig. 3c). 3D
20 analysis of the Φ_3 sample is shown in Fig. 3d (Zeiss[®] 3DSM software). An R_a value of 50 nm was found after
21 irradiation (about 10 nm before implantation). Thin sections of these samples were prepared by FIB and then
22 observed by TEM (Fig. 4).





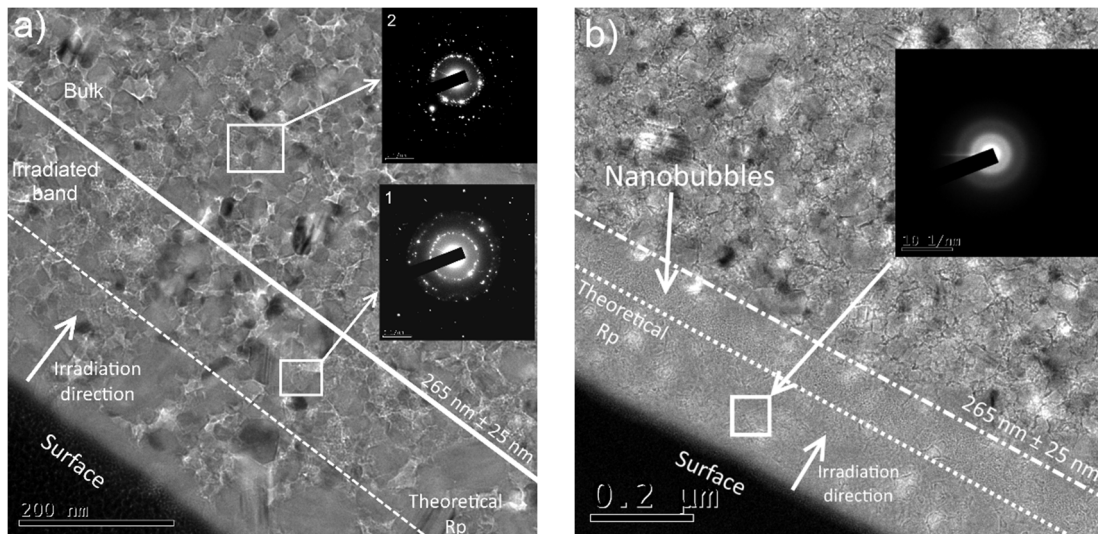
1



2

3

Figure 3: SEM images of the SiC surface after RT helium implantation at Φ_1 (a), Φ_2 (b) and Φ_3 (c). d) 3DSM analysis of the Φ_3 sample.



4

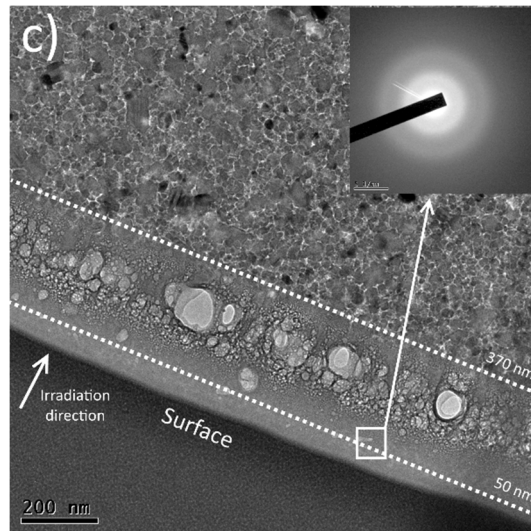


Figure 4: TEM image of the SiC sample after helium RT implantation at Φ_1 (a), Φ_2 (b) and Φ_3 (c).

In the case of Φ_1 , grain boundaries are clearly visible in the implanted area and no gas bubbles were formed near $R_p(\text{He})$ (Fig. 4a). SAED analysis (insert in Fig. 4a) confirmed that the material is still crystalline after implantation. Nevertheless, some crystalline disorder is observed in SAED pattern n°1 up to a depth of $265 \text{ nm} \pm 25 \text{ nm}$ (white line). For Φ_2 (Fig. 4b), nanometric bubbles are visible near the R_p (see also Fig. 10). **Smallest bubbles ($\sim 1 \text{ nm}$) need a slight defocus to be better observed. These appear light in underfocus and dark in overfocus and we assume these are full of helium and not voids.** The irradiated area is completely amorphous up to a depth of $265 \text{ nm} \pm 25 \text{ nm}$ (dash-dotted line in Fig. 4b), as indicated by the SAED pattern in Fig. 4b. Gas bubbles are also visible on Fig. 4c (Φ_3) and their sizes vary from a few nm on both sides of the implantation profile, to a maximum of $\sim 100 \text{ nm}$ in the area of maximum concentration. The bubble-containing band within the dotted lines is located at a depth of between 50 and 370 nm (see also Fig. 6), and the center of gravity of the largest bubbles is at a depth greater than the theoretical R_p calculated by SRIM, i.e. about 160 nm. The formation of large bubbles is responsible for surface swelling as shown on the TEM micrograph in Fig. 5 taken near the boundary between the irradiated and nonirradiated zones. The shift of implanted surface due to swelling with respect to the position of the non-implanted surface can reach 100 nm and this value gives a good indication of the height of the surface blisters observed in Fig. 3c.

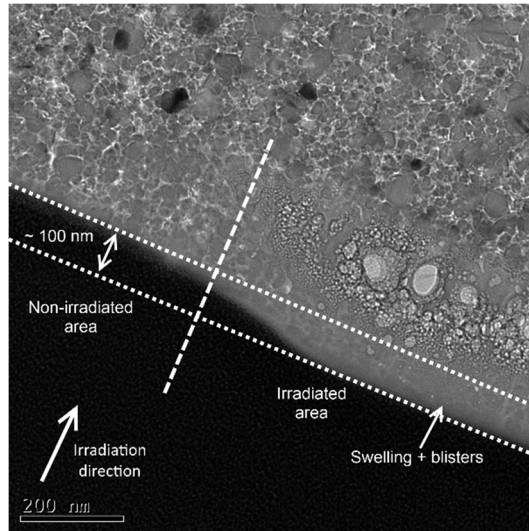


Figure 5: TEM image of He gas bubbles and surface swelling after irradiation at Φ_3 .

An attempt to segment the image using ImageJ software [46] was done based on the TEM micrograph of Fig. 6a. The corresponding binary image is given in fig. 6b.

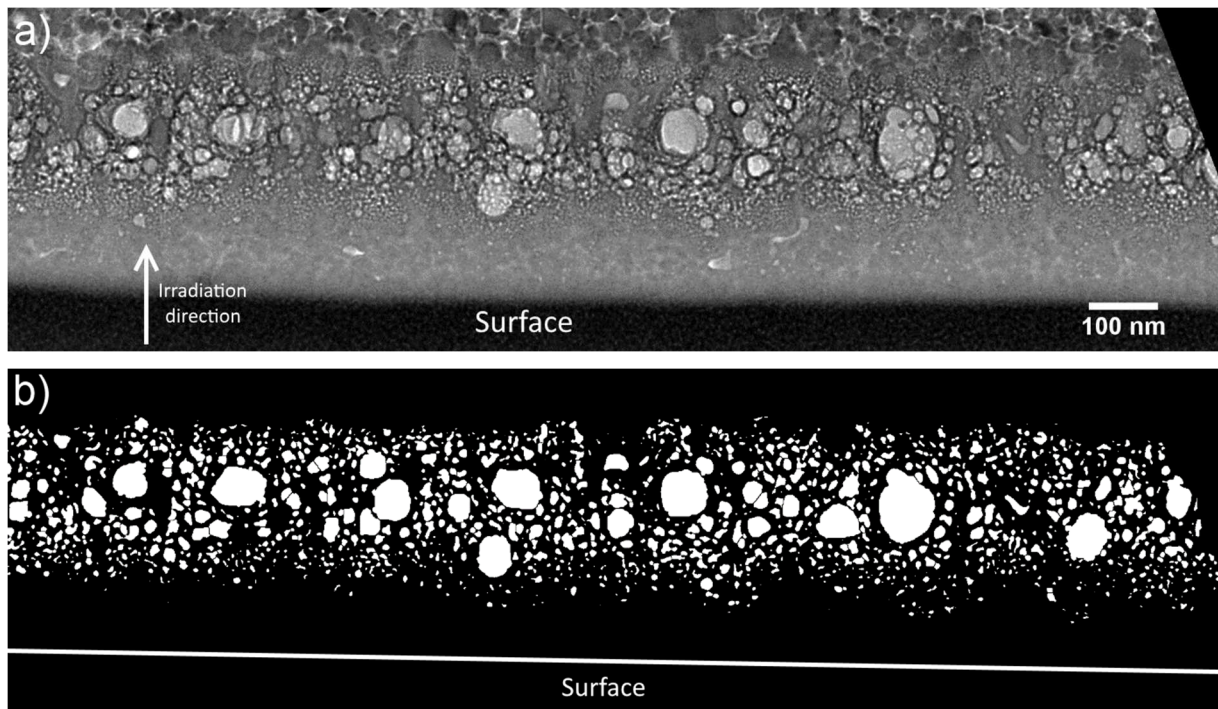
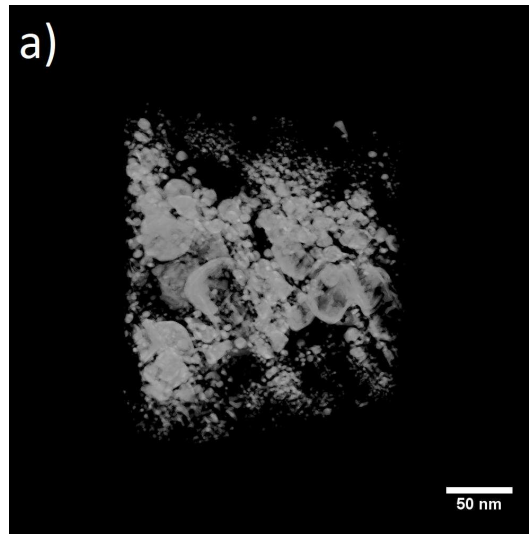


Figure 6: a) TEM image of SiC after helium RT-implantation Φ_3 and b) the corresponding binary image calculated using ImageJ software.

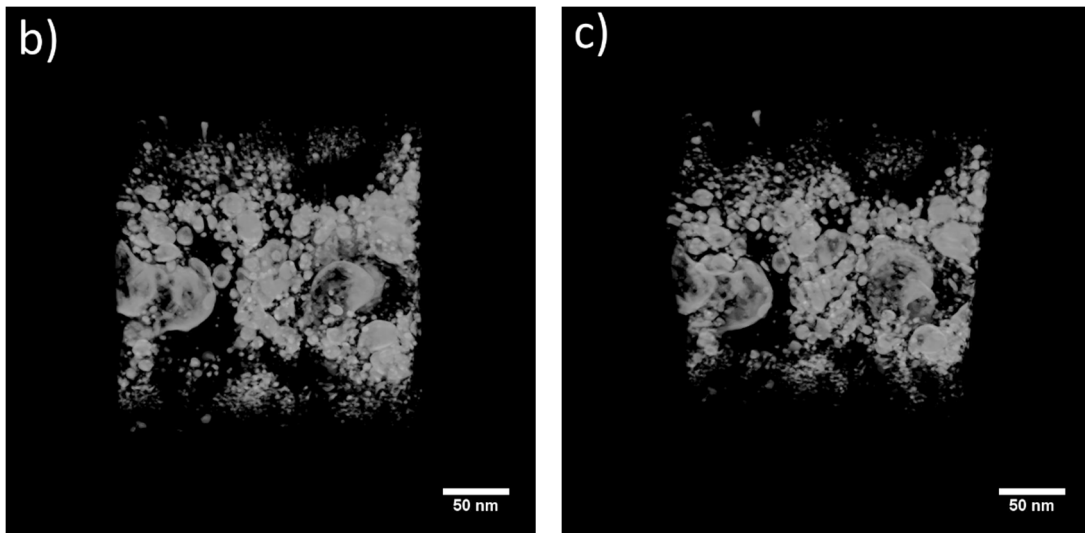
Measurement of bubble size as well as its eccentricity is difficult in this case because of the significant superposition of bubbles in the thickness of the FIB cross-section (about 100 nm). From this segmentation, bubbles have an average size of 9.2 ± 2.5 nm with a standard deviation of 9.3 nm. The latter reflects the large variety of bubble size. In addition, the low image contrast makes it difficult to take into account bubbles smaller than 1 or 2 nm. The average bubble size is therefore certainly overestimated here. Furthermore, no reliable eccentricity value

1 can be given, but from Fig. 6a, it appears that the bubbles appear to be relatively spherical. Therefore, both the
2 superposition of the bubbles on the thickness of the cross-section and the relative sphericity of those are better
3 visualized on Fig. 7a, b and c, obtained by electronic tomography.

4



5



6

7

Figure 7: a), b) and c): 2D projections at different angles of electron tomography analysis after implantation at Φ_3 .

8

9

3.2 Implanted area composition

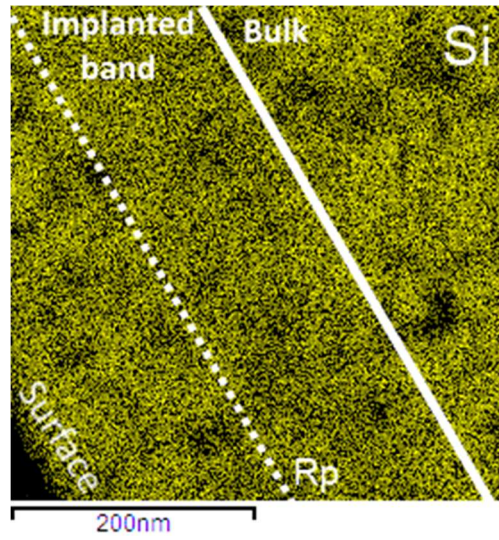
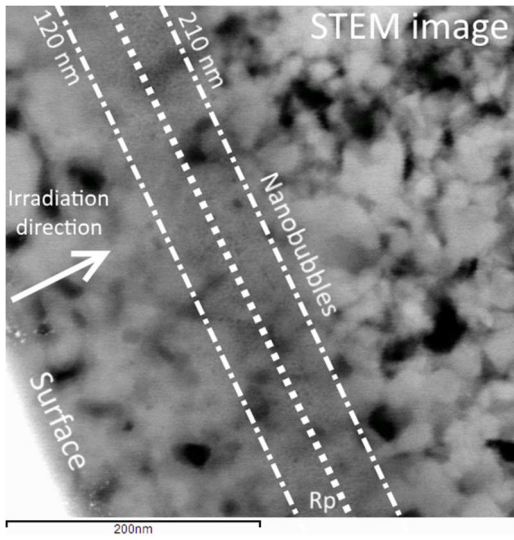
10

11

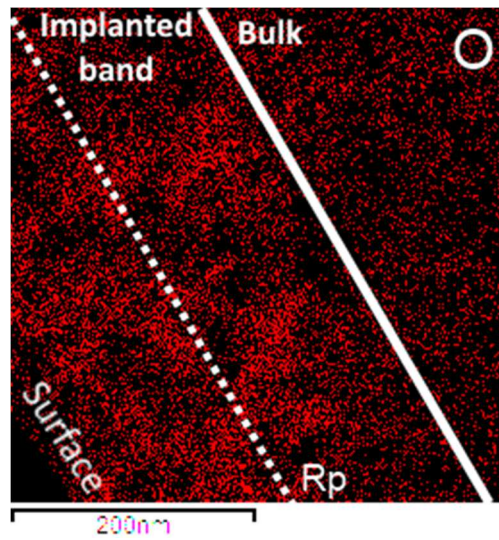
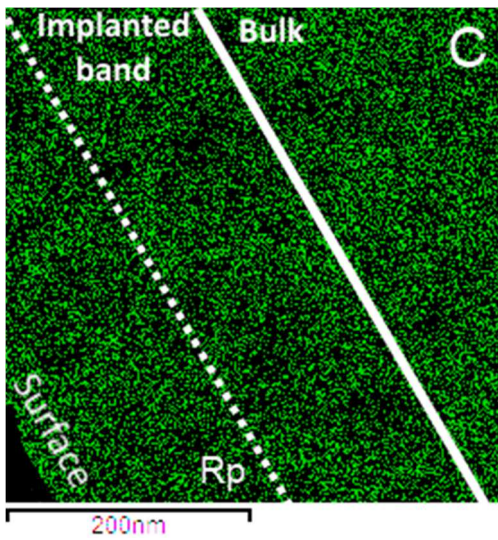
12

STEM-EDX analysis of the implanted area was performed. No noticeable changes in composition were observed for Φ_1 (not shown) and the resulting elemental mapping for Φ_2 and Φ_3 is shown in Fig. 8 and 9, respectively.

1



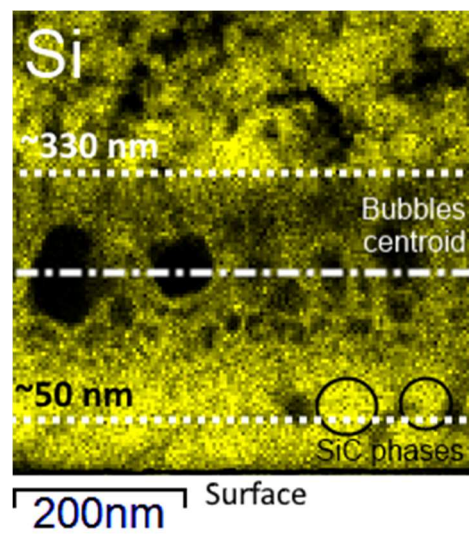
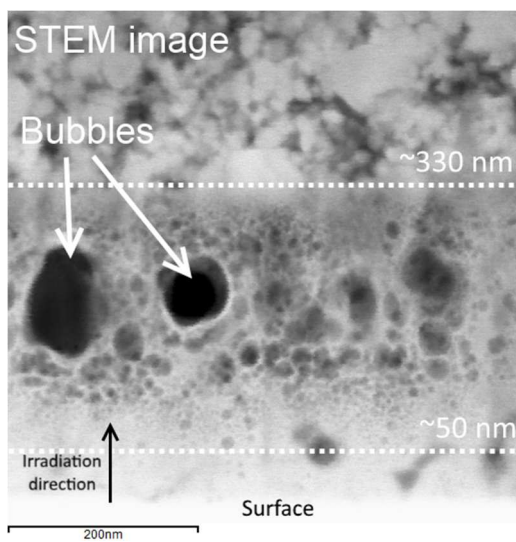
2

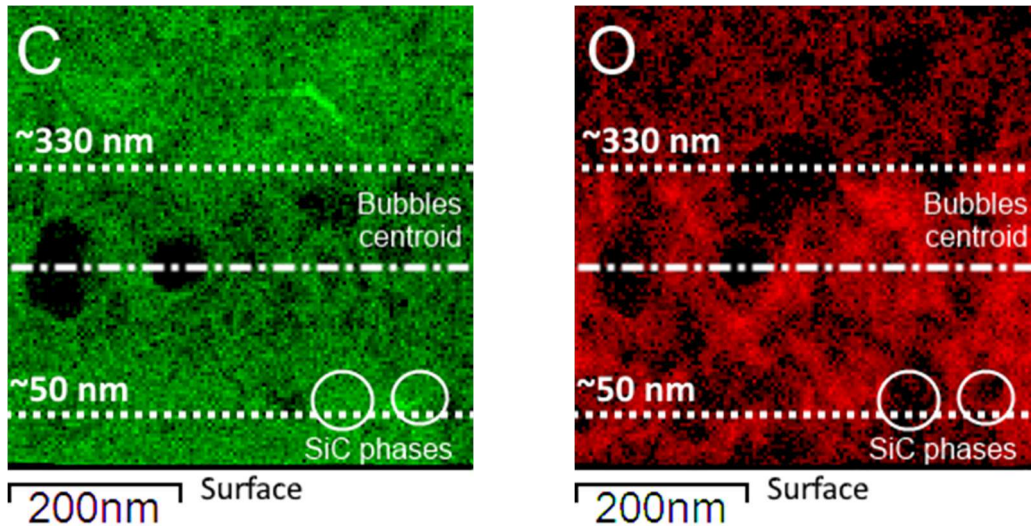


3

Figure 8: Elemental mapping of the implanted area obtained by STEM-EDX after helium irradiation at Φ_2 .

4



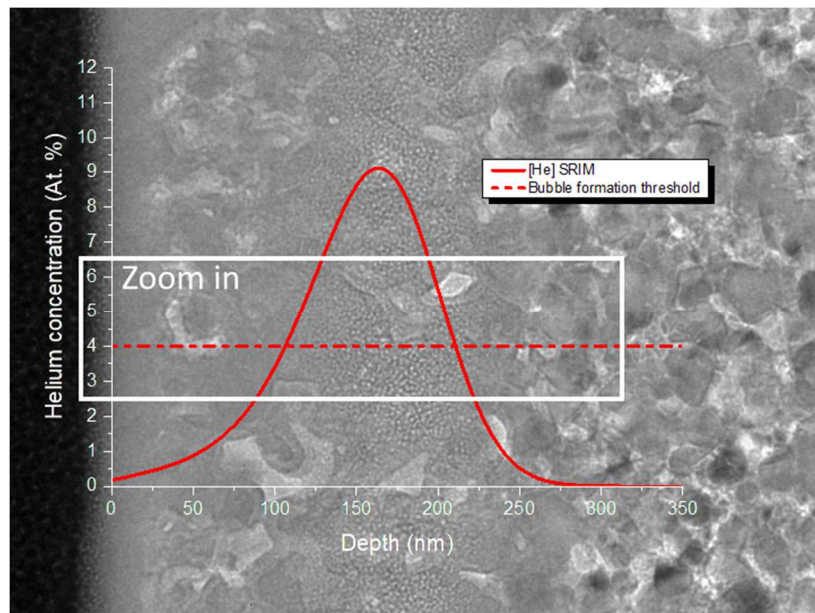


1
2
3
4
5
6
7
8
9

Figure 9: Elemental mapping of the implanted area obtained by STEM-EDX after helium irradiation at Φ_3 .

As can be seen from figures 8 and 9, the irradiation at Φ_2 and Φ_3 resulted in O-enrichment of the implanted area to a depth that also corresponds to the end of the band containing visible bubbles. This band extends from 120 to 210 nm for Φ_2 and from 50 to 330 nm for Φ_3 . However, some areas co-enriched in silicon and carbon and O-depleted still remain in the irradiated area (white circles in Fig. 9).

The theoretical helium profile at Φ_2 is superimposed on the STEM image in Fig. 10. The threshold of the helium concentration above which bubbles are formed can be estimated. It is found to be close to 4.0 at. % \pm 1 at. %.



10
11
12

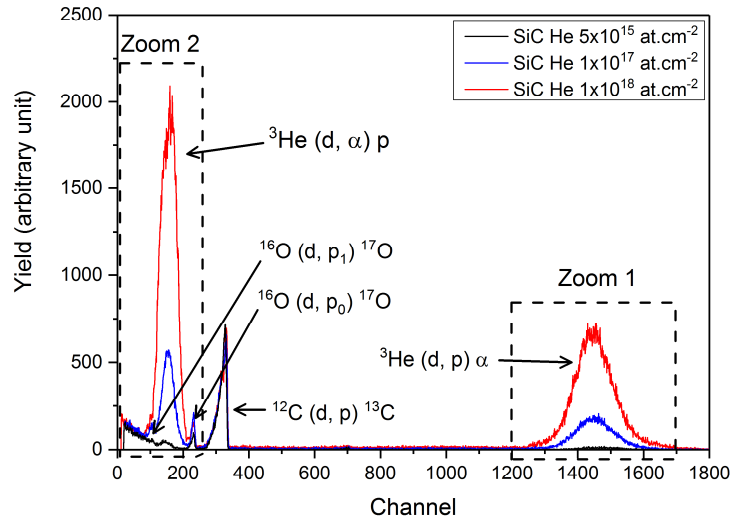
Figure 10: Superposition of the STEM micrograph and theoretical SRIM data at Φ_2 .

III-3 Helium profiles

1 Nuclear reaction analysis spectra obtained for each fluence are given in Fig. 11. Fig. 11b and 11c show
2 the zoomed in areas.

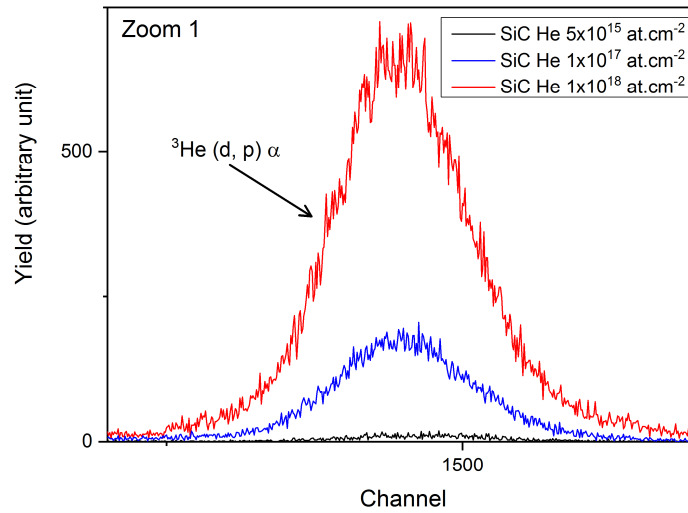
3

a)



4

b)



5

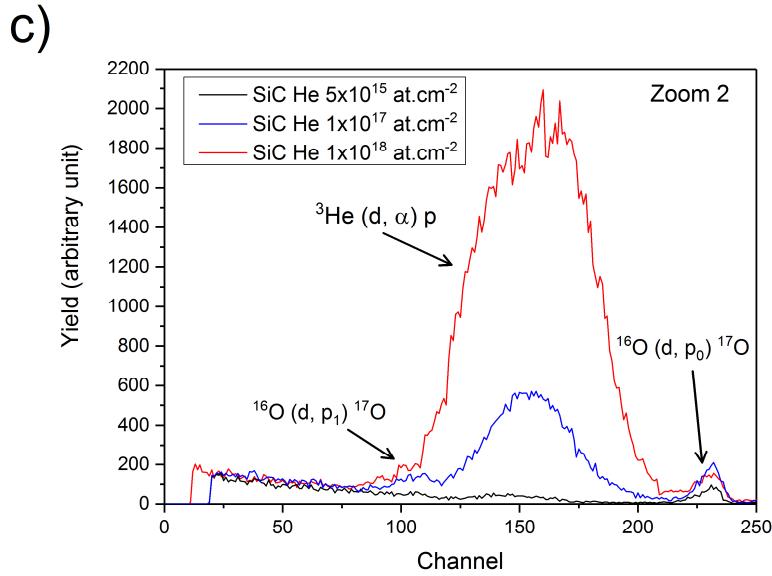


Figure 11: a) NRA spectrum for He implanted SiC, b) zoom on ³He (d, p) ⁴He reaction and c) zoom on low energy part of the spectrum

The signal corresponding to the ³He (d, p) ⁴He reaction (zoom 1) was integrated for the three fluences. The experimental ratios $\Phi_{\text{exp2}}/\Phi_{\text{exp1}}$ and $\Phi_{\text{exp3}}/\Phi_{\text{exp1}}$ were found to be 20 ± 5 and 73 ± 5 , respectively ($\Phi_{\text{th2}}/\Phi_{\text{th1}} = 20$ and $\Phi_{\text{th3}}/\Phi_{\text{th1}} = 200$). In the region of the (d, α) peak a signal associated with (d, p) reactions on oxygen is observed (Zoom 2). Indeed, the oxidation that was already visible on the STEM-EDX elemental mapping is confirmed here for the highest fluences. The (d, α) peak was integrated and the experimental ratios were found to be very close to the ones deduced previously from the ³He (d, p) ⁴He reaction i.e. 20 ± 5 and 69 ± 8 for $\Phi_{\text{exp2}}/\Phi_{\text{exp1}}$ and $\Phi_{\text{exp3}}/\Phi_{\text{exp1}}$, respectively. If one considers that the intensity of the (d, p) signal at Φ_1 is associated with the theoretical fluence of 5×10^{15} at.cm⁻², (no helium release expected at this fluence [47]), then Φ_{exp2} is close to 1×10^{17} at.cm⁻² whereas a value of 3.64×10^{17} at.cm⁻² is found for Φ_{exp3} , i.e. nearly 36.4 % of the theoretical fluence Φ_{th3} (1×10^{18} at.cm⁻²).

IV- Discussion

Helium irradiation at low fluence (Φ_1) does not cause material amorphization even at the dpa profile maximum which places the threshold of amorphization above 0.16 dpa in our experimental conditions. A certain degree of disorder is nevertheless created within the host matrix, symbolized by the visible halo on the diffractogram in Fig. 4a. At higher doses (Φ_2 and Φ_3), there is total amorphization of the material over a large band as expected for such dpa levels (see Fig. 1). The critical dose for amorphization in SiC at room temperature has been reported to be ~ 0.3 dpa for 1.5 MeV Xe ions [48] (concordant with an earlier study [39]), and ~ 1.1 -1.5 dpa for 20-70 keV He ions [43, 49]. The trend for the increase in dpa dose required with decreasing incident projectile mass, which has been reported previously by Snead et al. [50] is due to the decrease in residual chemical disorder per ion impact. Thus, more displacement damage is required to produce amorphization with lighter projectiles.

Irradiation at room temperature and at high fluence leads to a considerable oxidation of the material. This phenomenon may seem enigmatic since the irradiation is conducted under a controlled secondary vacuum. Oxygen uptake increases with the irradiation fluence as it was also observed on samples irradiated by xenon at room

1 temperature in a previous study [39]. Quantitative NRA analysis of irradiated surfaces confirmed the link between
 2 ion fluence and the uptake of oxygen by the material (Table 1).

Theoretical fluence	Dpa _{max}	Experimental helium fluence	Experimental oxygen fluence*
$\Phi_1^{\text{He}} = 5 \times 10^{15} \text{ at.cm}^{-2}$	0.16	$5 \times 10^{15} \text{ at.cm}^{-2}$	$< 3.40 \times 10^{14} \text{ at.cm}^{-2}$
$\Phi_2^{\text{He}} = 1 \times 10^{17} \text{ at.cm}^{-2}$	3.26	$1 \times 10^{17} \text{ at.cm}^{-2}$	$1.89 \times 10^{17} \text{ at.cm}^{-2}$
$\Phi_3^{\text{He}} = 1 \times 10^{18} \text{ at.cm}^{-2}$	32.6	$3.64 \times 10^{17} \text{ at.cm}^{-2}$	$2.97 \times 10^{17} \text{ at.cm}^{-2}$

3 *Table 1: Helium and oxygen fluences determined by nuclear reaction analysis. *NRA, Non-Rutherford cross-section [51]*

4 The question of the source of oxygen at the origin of this chemical evolution is worth asking. Two main
 5 hypotheses can be formulated according to whether one considers an “under beam” or “out of beam” oxidation.
 6 Oxygen incorporation in 4H-SiC during hydrogen implantation was already underlined by Barcz et al. [52]. These
 7 authors have shown that a cavity band near the end of range of hydrogen (or deuterium) tends to getter oxygen.
 8 They concluded that the oxygen most likely penetrates from the ambient (gaseous O₂ and H₂O molecules) by
 9 migrating from the sample edges along the heavily damaged and partially porous zone of damage produced by
 10 hydrogen implantation. In our case, the entire implanted area is oxidized and not only the area with helium cavities.
 11 It can be stipulated that the initial porosity of the material promotes the penetration of oxygen species that could
 12 come from the secondary vacuum in the irradiation chamber, the latter can never be considered perfect. This
 13 oxygen can also come partly from the oxide layer inevitably formed on the surface of SiC before irradiation.
 14 Another possibility is that oxidation occurs just after irradiation when the sample is vented. Indeed, the atmosphere
 15 then provides an abundant source of oxygen. A comprehensive study with a systematic parametric approach would
 16 be required to highlight the mechanics and key parameters involved in this process.

17 Up to a fluence of $1 \times 10^{17} \text{ at.cm}^{-2}$, no helium release was measured. However, a significant release of
 18 helium (about 70 %) was measured at the highest fluence Φ_3 . The remaining fluence of $3.64 \times 10^{17} \text{ at.cm}^{-2}$ could
 19 correspond to the saturation yield in our experimental conditions. Moreover, at this fluence, blisters form on the
 20 surface (around 100 nm in size) due to the presence of large bubbles beneath the surface. A threshold concentration
 21 of 4.0 at. % ± 1 at. % for the formation of helium bubbles was determined based on TEM observations. This value
 22 is in good agreement with the value reported by Zinkle et al. [30]. On the other hand, Harrison et al. [43], did not
 23 observed any He bubbles nucleation up to 5 dpa in the case of *in situ* experiments carried out on thin cross sections
 24 (~ 100 nm thick) in a TEM with 20 keV He at RT. In the latter case, however, the very specific experimental
 25 conditions perhaps explain such an apparent discrepancy. It is not clear whether oxidation, material amorphization
 26 and bubble formation are correlated phenomena or not in the present study. However, an instructive comparison
 27 can be done with another carbide (TiC) irradiated in similar conditions [40]. In this case, helium irradiation at Φ_3
 28 result in the formation of micro- or nano-cracks beneath the surface near the projected range (Fig. 12). As indicated
 29 by the SAED pattern, no amorphization occurred during ion implantation even if some disorder was present (insert
 30 in Fig. 12b). The accumulation of defect and gas at depth induces here a fracturing of the material rather than the
 31 formation of round bubbles. Almost no oxidation was measured in the irradiated TiC whatever the fluence. A
 32 possible conclusion could thus be that material amorphization favors oxygen incorporation in the case of SiC but
 33 this assumption may be confirmed by additional experiments (see next step below).

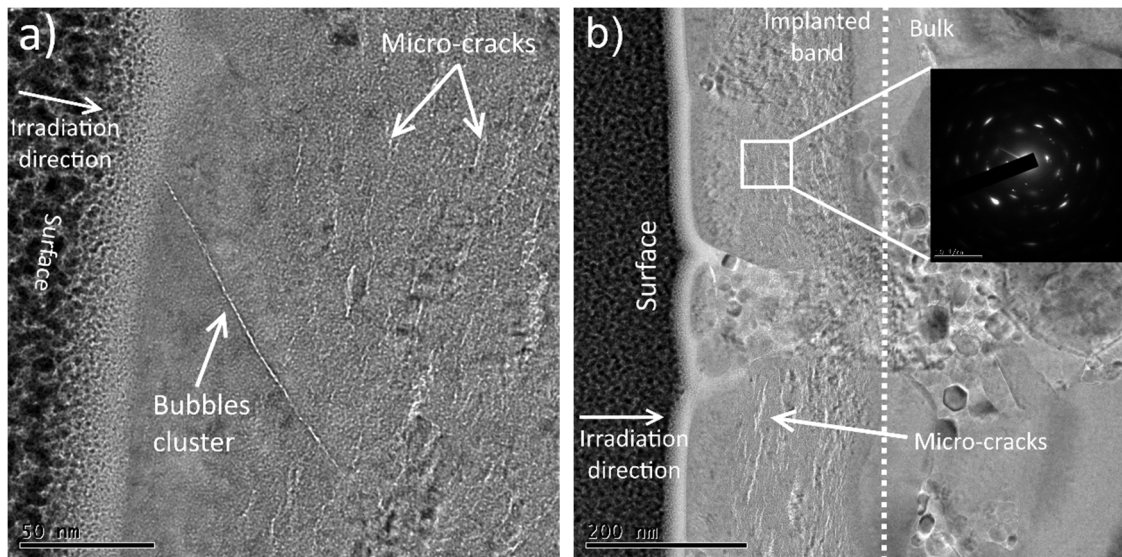


Fig. 12: TEM images of the TiC cross-section obtained by FIB after He RT-irradiation at a fluence of $\Phi_3 = 1 \times 10^{18} \text{ at.cm}^{-2}$.

In Fig. 12a, a grain boundary is present which appears to be decorated with bubbles outside the implanted He region by several tens of nanometers. Such segregation suggests enhanced He mobility in the grain boundary compared to the crystalline matrix and these could play a role in the release path for the implanted gas. Indeed, about 80% of helium is released from TiC after RT implantation at Φ_3 . This loss is higher than for SiC implanted in similar conditions (about 70%). Note that the mechanism at the origin of helium release is still unclear in the case of SiC. In Fig. 4c, most bubbles are located at a depth comprised between 100 and 340 nm. Almost no bubbles are observed in the first 100 nm and the surface blisters are closed for the most part which prevents the formation of visible outlets for the release of the gas. Bubble emptying is thus suspected, possibly including helium redissolution and a diffusion step through the amorphous SiC layer.

The next step of this work will consist in using different thermal treatments during implantation. Irradiation experiments at temperatures between 300 and 1000 °C (to preserve SiC crystallinity) will be performed as a follow-up to this study. A similar protocol will be applied at RT and at high temperature on CVD deposits. Indeed, the advantage of CVD technique (epitaxial growth) over HP or SPS sintering is that it allows a reproducible deposition of very fine microstructures (grain size $\ll 100 \text{ nm}$ and down to a few nanometers) without classical manufacturing bias: very high densification rate, no porosity and composition / quasi-perfect stoichiometry.

V- Conclusion

β -SiC sintered bodies were implanted with 30 keV ^3He ions at room temperature and up to an ion fluence of $1 \times 10^{18} \text{ cm}^{-2}$. Nanometric bubbles are formed after irradiation at $10^{17} \text{ at.cm}^{-2}$ and the threshold concentration for their formation is estimated at $\sim 4.0 \text{ at. \%}$. Virtually no helium release is measured below $10^{17} \text{ at.cm}^{-2}$ by NRA technique. For the highest fluence, the maximum size of bubbles reaches a hundred nanometers and surface blistering is observed. Approximately 70% of the helium is released during implantation and the irradiated zone also undergoes significant oxidation. The link between the microstructural evolution of the material, its progressive oxidation under beam and the release of helium is discussed. The very likely role played by the porosity on the

1 oxidation of the material under irradiation at RT is underlined. Finally, a penetration of oxygen by migrating from
2 the porosities through the heavily damaged area seems to be the most likely hypothesis.

3

4 Acknowledgments:

5 SEM and TEM images were made using the CT μ facilities (Technological Center of Microstructures:
6 <http://microscopies.univ-lyon1.fr/>) in the Université de Lyon (France). Our many thanks also go to D. Troadec
7 from the IEMN laboratory (Lille, France) for the fabrication of thin cross-sections. This work has been carried out
8 within the framework of the EUROfusion Consortium and French Research Federation for Fusion Studies and has
9 received funding from the Euratom research and training programme 2014–2018 under grant agreement No.
10 633053. The views and opinions expressed herein do not necessarily reflect those of the European Commission.

11

12 References

13 [1]: C. H. Carter Jr, R. F. Davis, J. Bentley, “Kinetics and Mechanisms of High-Temperature Creep in
14 Silicon Carbide: II, Chemically Vapor Deposited”, *J. Am. Ceram. Soc.* 67 (1984) 732.

15 [2]: V. Angelici Avincola, M. Grosse, U. Stegmaier, M. Steinbrueck, H. J. Seifert, “Oxidation at high
16 temperatures in steam atmosphere and quench of silicon carbide composites for nuclear application”,
17 *Nucl. Eng. Des.* 295 (2015) 468.

18 [3]: B. A. Pint, K. A. Terrani, M. P. Brady, T. Cheng, J. R. Keiser, “High temperature oxidation of
19 fuel cladding candidate materials in steam–hydrogen environments”, *J. Nucl. Mater.* 440 (2013) 420.

20 [4]: L. L. Snead, T. Nozawa, M. Ferraris, Y. Katoh, R. Shnavski, M. Sawan, “Silicon Carbide
21 Composites as Fusion Power Reactor Structural Materials”, *J. Nucl. Mater.* 417 (2011) 330.

22 [5]: W. J. Kim, S. M. Kang, K. H. Park, A. Kohyama, W. S. Ryu, J. Y. Park, “Fabrication and ion
23 irradiation of SiC-based ceramics for advanced nuclear energy systems”, *J. Korean Ceram. Soc.* 42
24 (2005) 575.

25 [6]: L. L. Snead, T. Nozawa, Y. Katoh, T. S. Byun, S. Kondo, D. A. Petti, “Handbook of SiC
26 properties for fuel performance modeling”, *J. Nucl. Mater.* 371 (2007) 329.

27 [7]: Y. Katoh, A. Kohyama, T. Nozawa, M. Sato, “SiC/SiC Composites Through Transient Eutectic-
28 Phase Route for Fusion Applications” *J. Nucl. Mater.* 587 (2004) 329.

29 [8]: Y. Katoh, L. L. Snead, C. H. Henager, A. Hasegawa, A. Kohyama, B. Riccardi, “Current status
30 and critical issues for development of SiC composites for fusion applications” *J. Nucl. Mater.* 659
31 (2007) 367.

- 1 [9]: Y. Katoh, L. L. Snead, T. Cheng, C. Shih, W. D. Lewis, T. Koyanagi, T. Hinoki, C. H. Henager
2 Jr, M. Ferraris, “Radiation-tolerant joining technologies for silicon carbide ceramics and composites”,
3 J. Nucl. Mater. 448 (2014) 497.
- 4 [10]: Y. Katoh, K. Ozawa, C. Shih, T. Nozawa, R. J. Shinavski, A. Hasegawa, L. L. Snead,
5 “Continuous SiC fiber, CVI SiC matrix composites for nuclear applications: Properties and irradiation
6 effects” J. Nucl. Mater. 448 (2014) 448.
- 7 [11]: F. Linez, E. Gilabert, A. Debelle, P. Desgardin, M.-F. Barthe, “Helium interaction with vacancy-
8 type defects created in silicon carbide single crystal” J. Nucl. Mater. 436 (2013) 150.
- 9 [12]: T. Koyanagi, K. Ozawa, T. Hinoki, K. Shimoda, Y. Katoh, “Effects of neutron irradiation on
10 mechanical properties of silicon carbide composites fabricated by nano-infiltration and transient
11 eutectic-phase process”, J. Nucl. Mater. 448 (2014) 478.
- 12 [13]: L. Q. Zhang, C. H. Zhang, L. H. Han, C. L. Xu, J. J. Li, Y. T. Yang, Y. Song, J. Gou, J. Y. Li, Y.
13 Z. Ma, “Surface damage on 6H-SiC by highly-charged Xeq+ ions irradiation”, J. Nucl. Mater. 455
14 (2014) 704.
- 15 [14]: Q. Wang, C. Wang, Y. Zhang, T. Li, “Molecular dynamics study on interfacial thermal
16 conductance of unirradiated and irradiated SiC/C”, Nucl. Instrum. Meth. B 328 (2014) 42.
- 17 [15]: T. J. Gerczak, G. Zheng, K. G. Field, T. R. Allen, “Effect of exposure environment on surface
18 decomposition of SiC–silver ion implantation diffusion couples”, J. Nucl. Mater. 456 (2015) 281.
- 19 [16]: L. L. Snead, K. A. Terrani, Y. Katoh, C. Silva, K. J. Leonard, A. G. Perez-Bergquist, “Stability
20 of SiC-matrix microencapsulated fuel constituents at relevant LWR conditions” J. Nucl. Mater. 448
21 (2014) 389.
- 22 [17]: D. Guo, H. Zang, P. Zhang, J. Xi, T. Li, L. Ma, C. He, “Analysis of primary damage in silicon
23 carbide under fusion and fission neutron spectra”, J. Nucl. Mater. 455 (2014) 229.
- 24 [18]: N. Chaâbane, M. Le Flem, M. Tanguy, S. Urvoy, C. Sandt, P. Dumas, Y. Serruys, “Au ion
25 irradiation of various silicon carbide fiber-reinforced SiC matrix composites”, J. Nucl. Mater. 439
26 (2013) 123.
- 27 [19]: G. M. Wright, M. G. Durrett, K. W. Hoover, D.G. Whyte, L. A. Kesler, “Silicon Carbide as a
28 tritium permeation barrier in tungsten plasma-facing components”, J. Nucl. Mater. 458 (2015) 272.
- 29 [20]: C. Soto, C. García-Rosales, J. Echeberria, J. M. Martínez-Esnaola, T. Hernández, M. Malo, E.
30 Platacis, F. Muktepavela, “SiC-based sandwich material for Flow Channel Inserts in DCLL blankets:
31 Manufacturing, characterization, corrosion tests”, Fus. Eng. Des. 124 (2017) 958.

- 1 [21]: A. Ivekovic, S. Novak, G. Drazic, D. Blagoeva, S. Gonzalez de Vicente, "Current status and
2 prospects of SiCf/SiC for fusion structural applications", *J. Eur. Ceram. Soc.* 33 (2013) 1577.
- 3 [22]: H. L. Heinisch, L. R. Greenwood, W. J. Weber, R. E. Williford, "Displacement damage in
4 silicon carbide irradiated in fission reactors", *J. Nucl. Mater.* 327 (2004) 175.
- 5 [23]: R. H. Jones, L. Giancarli, A. Hasegawa, Y. Katoh, A. Kohyama, B. Riccardi, L. L. Snead, W. J.
6 Weber, "Promise and challenges of SiCf/SiC composites for fusion energy applications", *J. Nucl.*
7 *Mater.* 307-311 (2002) 1057.
- 8 [24]: E. E. Bloom, S. J. Zinkle, F. W. Wiffen, "Materials to deliver the promise of fusion power:
9 progress and challenges", *J. Nucl. Mater.* 329-333 (2004) 12.
- 10 [25]: L. L. Snead, R. H. Jones, A. Kohyama, P. Fenici, "Status of silicon carbide composites for
11 fusion" *J. Nucl. Mater.* 233-237 (1996) 26.
- 12 [26]: T. Yano, Y. Futamura, S. Yamazaki, T. Sawabe, K. Yoshida, "Recovery behavior of point
13 defects after low-dose neutron irradiation at 423K of sintered 6H-SiC by lattice parameter and
14 macroscopic length measurements", *J. Nucl. Mater.* 442 (2013) S399.
- 15 [27]: F. Linez, F. Garrido, H. Erramli, T. Sauvage, B. Courtois, P. Desgardin, M.-F. Barthe,
16 "Experimental location of helium atoms in 6H-SiC crystal lattice after implantation and after
17 annealing at 400°C", *J. Nucl. Mater.* 459 (2015) 62.
- 18 [28]: C. H. Zhang, S. E. Donnelly, V. M. Vishnyakov, J. H. Evans, "Dose dependence of formation of
19 nanoscale cavities in helium-implanted 4H-SiC", *J. Appl. Phys.* 94 (2003) 6017.
- 20 [29]: B. S. Li, C. H. Zhan, H. H. Zhang, T. Shibayama, Y. T. Yang, "Study of the damage produced in
21 6H-SiC by He irradiation", *Vacuum* 86 (2011) 452.
- 22 [30]: S. J. Zinkle, "Effect of H and He irradiation on cavity formation and blistering in ceramics",
23 *Nucl. Instrum. And Meth. B* 286 (2012) 4.
- 24 [31]: J. Chen, P. Jung, H. Ullmaier, "Stresses, strains and cracks in a helium-implanted SiC/C
25 composite" *J Nucl Mater* 336 (2005) 194.
- 26 [32]: C. Tromas, V. Audurier, S. Leclerc, M. F. Beaufort, A. Declémy, J. F. Barbot, "Evolution of
27 mechanical properties of SiC under helium implantation", *Nucl Instr. Meth B* 266 (2008) 2776.
- 28 [33]: K. Hojou, S. Furuno, K. N. Kushita, N. Sasajima, K. Izui, "EELS analysis of SiC crystals under
29 hydrogen and helium dual-ion beam irradiation", *Nucl Instr. Meth B* 141 (1998) 148.

- 1 [34]: M. Sasase, Y. Ito, K. Yasuda, R. Ishigami, S. Hatori, A. Yamamoto, “Defect formation in 6H-
2 SiC irradiated by 3 MeV He ions”, Nucl Instr. Meth B 209 (2003) 179.
- 3 [35]: S. Leclerc, M. F. Beaufort, A. Declémy, J. F. Barbot, “Damage induced in high energy helium-
4 implanted 4H-SiC”, Nucl Instr. Meth B 242 (2006) 399.
- 5 [36] Q. Shen, G. Ran, W. Zhou, C. Ye, Q. Feng and N. Li, “Investigation of Surface Morphology of
6 6H-SiC Irradiated with He⁺ and H₂⁺ ions”, Materials 11 (2008) 60
- 7 [37]: G. Velisa, A. Debelle, L. Thome, S. Mylonas, L. Vincent, A. Boulle, J. Jagielski, D. Pantelica,
8 “Implantation of high concentration noble gases in cubic zirconia and silicon carbide: A contrasted
9 radiation tolerance”, J. Nucl. Mater. 451 (2014) 14.
- 10 [38]: L. Jamison, K. Sridharan, S. Shannon, I. J. Szlufarska, “Temperature and irradiation species
11 dependence of radiation response of nanocrystalline silicon carbide”, Mater. Res. 29 (2014) 2871–
12 2880.
- 13 [39]: J. Baillet, S. Gavarini, N. Millard-Pinard, V. Garnier, C. Peaucelle, X. Jaurand, A. Duranti, C.
14 Bernard, R. Rapegno, S. Cardinal, L. Escobar Sawa, T. De Echave, B. Lanfant, Y. Leconte, J. Nucl.
15 Mater. 503 (2018) 140.
- 16 [40]: PhD work of J. Baillet, Comportement du xénon et de l'hélium dans le carbure de silicium :
17 applications au domaine de l'énergie nucléaire (fission et fusion) (2013–2016): [https://tel.archives-
18 ouvertes.fr/tel-01484791](https://tel.archives-ouvertes.fr/tel-01484791)
- 19 [41]: B. Lanfant, Y. Leconte, G. Bonnefont, V. Garnier, Y. Jorand, S. LeGallet, M. Pinault, N. Herlin-
20 Boime, F. Bernard, G. Fantozzi, “Effects of carbon and oxygen on the spark plasma sintering additive-
21 free densification and on the mechanical properties of nanostructured SiC ceramics”, J. Eur. Ceram.
22 Soc. 35 (2015) 3369.
- 23 [42]: J. F. Ziegler, J. P. Biersack, M. D. Ziegler, The Stopping and Range of Ions in Matter, SRIM Co,
24 2008. www.SRIM.org.
- 25 [43]: R. W. Harrison, S. Ebert, J. A. Hink, S. E. Donnelly, “On the fabrication of ZrC_xNy from
26 ZrO₂ via two-step carbothermic reduction–nitridation”, J. Eur. Ceram. Soc. 38 (2018) 3718.
- 27 [44]: L. Zhang, W. Jiang, A. Dissanayake, T. Varga, J. Zhang, Z. Zhu, D. Hu, H. Wang, C. H.
28 Henager Jr, and T. Wang, “Grain growth of nanocrystalline 3C-SiC under Au ion irradiation at
29 elevated temperatures”, J. Phys. D: Appl. Phys. 49 (2016) 035304.
- 30 [45]: H. S. Bosch, G. M. Hale, “Improved formulas for fusion cross sections and thermal reactivities”,
31 Nucl. Fus. 32 (1992) 611.

- 1 [46]: W. S. Rasband, ImageJ, U. S, National Institutes of Health, Bethesda, Maryland, USA, 1997-
2 2016. <http://imagej.nih.gov/ij/>.
- 3 [47]: P. Trocellier, S. Miro, Y. Serruys, S. Vaubailon, S. Pellegrino, S. Agarwal, S. Moll, L. Beck,
4 “Study of helium migration in nuclear materials at Jannus–Saclay”, Nucl Instr. Meth B 331 (2014) 55.
- 5 [48]: W. J. Weber, L. M. Wang, N. Yu, “The irradiation-induced crystalline-to-amorphous phase
6 transition in α -SiC”, Nucl. Instrum. Methods Phys. Res. B 116 (1–4) (1996) 322–326.
- 7 [49]: M. Liu, X. Yang, Y. Gao, R. Liu, H. Huang, X. Zhou, T. K. Sham, “Investigation of the damage
8 behavior in CVD SiC irradiated with 70keV He ions by NEXAFS, Raman and TEM”, J. Eur. Ceram.
9 Soc. 37 (4) (2017) 1253.
- 10 [50]: L. L. Snead, S. J. Zinkle, W. S. Eatherly, D. K. Hensley, N. L. Vaughn, J. W. Jones, “Dose Rate
11 Dependence of the Amorphization of Silicon Carbide”, MRS Proc. 540 (1998).
- 12 [51]: A. Chevarier, N. Chevarier, M. El Bouanani, E. Gerlic, M. Stern, B. Roux, F. Thimon, “Profiling
13 of carbon, oxygen and argon contamination in sputter-deposited films using nuclear backscattering
14 and nuclear reaction spectroscopy”, Appl. Surf. Sci. 215 (1991) 48.
- 15 [52]: A. Barcz, R. Jakiela, M. Kozubal, J. Dyczewski, G. K. Celler, “Incorporation of oxygen in SiC
16 implanted with hydrogen”, Nucl Instr. Meth B 365 (2015) 146–149.
- 17